communications physics

A Nature Portfolio journal

Article

https://doi.org/10.1038/s42005-025-02362-0

Transient chirality in the gelation of adhesive spinner monolayers

Yujie Jiang [1] ✉, Haiquan Li[2], Yiting Liu[3], Haoran Li[3] & Yang Cui[3]

Active systems of self-rotating elements inherently exhibit chirality, making them of fundamental interest due to parity violation. Yet how rotational activity influences gelation and whether such chirality can persist into the arrested state remain unclear. Using large-scale hydrodynamic simulations, we investigate the gelation of adhesive spinners confined to quasi-2D monolayers at low Reynolds numbers. Unlike the coarsening dynamics of passive colloids, spinner gelation follows a different pathway, displaying structural chirality during the early stages of aggregation. However, this chirality dissipates upon dynamical arrest, resulting in a final gel structure that resembles a conventional colloidal gel. As a result, we find no sign of odd mechanical responses. Nonetheless, the elastic modulus and gelation time remain tunable through spinning activity, providing a potential avenue for the bottom-up design of programmable soft materials.

Soft particulate gels are ubiquitous in industrial applications, ranging from daily consumer products to pharmaceuticals and biotechnology[1–3]. These gels usually form when attractive colloidal particles undergo Brownian motion, aggregate into open clusters, and eventually percolate throughout the system, i.e., the colloidal gel[4,5]. The resulting porous network imparts unique mechanical and rheological properties[6,7]. While non-equilibrium protocols, such as thermal annealing[8] and external flow[9], have been developed to tune gel structures, recent studies combine active matter and particulate gels to achieve programmable properties[10–13]. For instance, self-propelled active particles have been utilized to regulate mesoscale dynamics and, consequently, the structure within gels through local energy injection[14].

Beyond directional swimmers, spinners—particles driven by an active torque—also constitute an important class of active matter[15–17]. These systems typically operate in hydrodynamic environments, which, in the absence of Brownian diffusion, enable translational motion at a collective level[18]. The inherent chirality of rotational dynamics gives rise to diverse self-assembly behaviors and collective motions[12,19,20]. Moreover, the resulting non-reciprocal interactions can lead to unique, parity-violating odd responses, such as odd viscosity[21] and Hall-like effect[22]. While extensive research has been conducted on chiral active fluids[19,23,24], the interplay between rotational activity and gelation remains less explored, despite its scientific significance as highlighted in recent works[12,25].

In this study, we employ large-scale hydrodynamic simulations to investigate the gelation of adhesive spinners under inertialess conditions. The system is confined to quasi-2D (i.e., monolayers) to accentuate chiral effects. Our simulation scheme couples the Lattice Boltzmann Method (LBM) with the Discrete Element Method (DEM)[26], incorporating lubrication corrections to fully resolve fluid-solid interactions. Conventional colloidal gelation proceeds via arrested phase separation, where spinodal decomposition textures are dynamically arrested at a percolating state[27]. Unlike passive colloids, spinning rotors do not undergo diffusive motion, making it intriguing to examine the emergence of chirality and its potential contribution to odd mechanics. Mechanical metamaterials with chiral unit cells display anomalous responses[28–30], motivating the fundamental question of whether dynamical chirality (self-rotation) can convert into persistent structural chirality during gelation, and whether such symmetry breaking continues to affect rheology after spinning activity ceases. We find that adhesive spinners gel through a different route, yet end up with a similar mesoscale structure to colloidal gels, irrespective of spinning activity. Transient structural chirality arises during early-stage clustering yet dissipates as clusters merge into a percolating network, resulting in isotropic final structures and rheology. However, the elastic modulus and gelation rate vary as functions of spinning activity, suggesting a practical approach to tailoring particulate gels.

Results

System characterization

Our system comprises N spherical spinners (of diameter d) suspended in a Newtonian fluid (of viscosity η and density ρ). These particles are confined within a thin square simulation box with lateral dimensions $L_{x,y} = 120d$, which is sufficiently large to eliminate finite size effect (see Supplementary Note 1), and height $h = 3d$ along the z-axis, Fig. 1a. Each spinner experiences an active torque T_a applied along the $-z$ direction, inducing clockwise self-rotation. While periodic boundaries are applied to the x- and y-directions, we introduce two flat walls at $z = 0$ and $z = h$, and confine the particles to the bottom monolayer at $z = 0.5d$. This setup mimics experimental conditions

[1]School of Mathematics and Physics, University of Science and Technology Beijing, Beijing, China. [2]School of Mechanical Engineering, University of Science and Technology Beijing, Beijing, China. [3]21C LAB, Contemporary Amperex Technology Company, Limited, Ningde, China. ✉e-mail: yjjiang@ustb.edu.cn

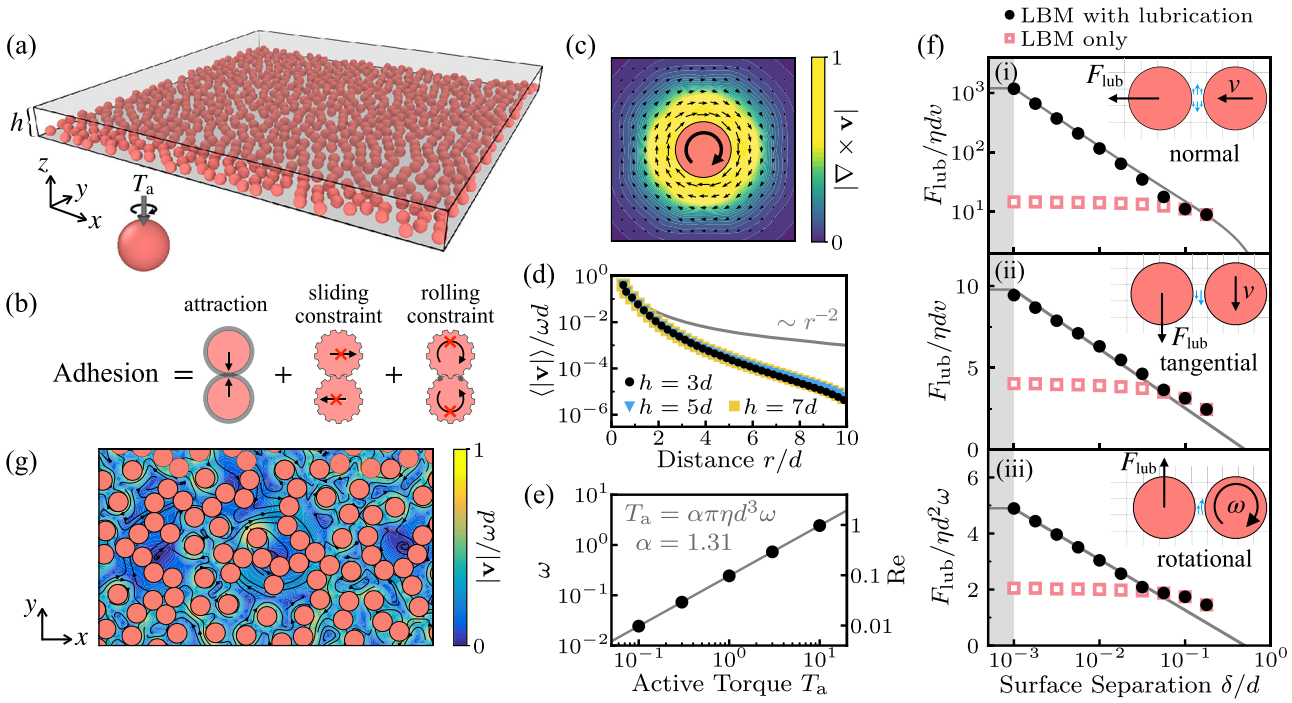

Fig. 1 | Simulation setup. a Simulation setup of the quasi-2D spinner monolayer. **b** Adhesion model depicting the central attractive force and tangential constraints, including sliding and rolling resistance. **c** Flow field in the *x*-*y* plane at $z = 0.5d$ (d: particle diameter), showing velocity vectors (arrows) and vorticity (color map) around an isolated spinner. **d** Normalized velocity profiles as a function of radial distance r/d at different box heights h. The solid gray line represents $\langle|\mathbf{v}|\rangle/\omega d = 0.125r^{-2}$, where $\mathbf{v}$ refers to fluid velocity and ω to particle angular speed. **e** Angular velocity ω as a function of active torque T_a. Linear fitting (solid gray line) yields $T_a = \alpha\pi\eta d^3\omega$ (η: fluid viscosity) with $\alpha = 1.31$ as a shifted factor. **f** Comparison of lubrication forces F_{lub} between simulations with lubrication corrections (black) and without lubrication corrections (pink). The two circles represent particles with relative motions of normal approach (i), tangential sliding (ii), and rotation (iii). Solid gray lines denote theoretical predictions[34]. The shaded region ($\delta < 10^{-3}d$) indicates the inner cutoff of the lubrication model. **g** Snapshot of spinner monolayer with area fraction $\phi = 0.4$ during gelation. Curved arrows indicate flow streamlines, while the color map represents velocity magnitude.

where density-mismatched particles, such as the hematite beads[31,32], sediment onto a substrate. For simplicity, we consider isotropic adhesion instead of complex interactions (such as magnetic-dipolar forces), allowing for a more fundamental scope. The adhesion applies within a short range ($\zeta_a = 0.01d$), consisting of central attraction, tangential friction, and rolling resistance, Fig. 1b. All three components are depicted by modified Hookean models with a unified spring constant k, which is sufficiently large ($U_{adh} \equiv \frac{1}{2}k\zeta_a^2 \gg T_a$) to ensure strong adhesion. As a result, relative motions between adhered particles are effectively constrained.

The dynamics of the adhesive spinners are implemented in DEM using LAMMPS[33], while hydrodynamic interactions are captured using LBM. To balance efficiency and accuracy, we set the LBM lattice spacing to $\Delta x = 0.25d$, which provides minimal yet sufficient resolution to reproduce the Stokes drag on a single-particle level. Within this resolution, lubrication corrections are applied between particle pairs without compromising accuracy, Fig. 1f. By setting an inner cutoff $10^{-3}d$ to prevent divergence at contact, this simulation scheme well captures both near- and far-field hydrodynamics. More simulation details can be found in the "Methods" section.

The flow field surrounding an isolated spinner, Fig. 1c, exhibits a radial decay. Figure 1d shows that the decay of the averaged velocity $\langle|\mathbf{v}|\rangle$ is faster than an expected inverse square law[34], likely due to additional hydrodynamic resistance from the no-slip walls (particularly the bottom one). In this work, we use a thin simulation box with a height of $h = 3d$, which yields velocity profiles similar to those obtained with larger h, Fig. 1d. The rotation speed ω is proportional to the applied torque T_a, and a linear fit to $T_a = T_a(\omega)$ reveals a shift factor of $\alpha = 1.31$ from the Stokes law, Fig. 1e. This deviation also arises from the no-slip bottom wall.

To manifest the role of chirality in gelation, we systematically eliminate potential confounding factors. Our spinners are athermal so that all motion is solely caused by self-rotation. The Reynolds number, defined as $\mathrm{Re} \equiv \omega\rho d^2/\eta = 0.1$, is sufficiently low to suppress inertial effects such as levitation[35] and secondary flows[36]. Hydrodynamic repulsion due to the Magnus effect[20] is also negligible. The area fraction $\phi \equiv N\pi d^2/4L_xL_y$ is mainly fixed at 0.4, while we also probe the system from $\phi = 0.3$ to 0.5. Simulations are initialized with a random configuration without overlap, and evolve for $50 \times 2\pi/\omega$ (i.e., 50 laps) until reaching a steady state.

Spinner gelation

As particles spin and agitate the surrounding fluid, the consequent flow in turn drives spinners to move translationally and aggregate under adhesive interactions, Fig. 1g. For small clusters, the summed active torque causes them to rotate collectively around their center of mass, while adhesion restricts internal relative motion. More spinners then adhere to the periphery of these clusters, forming chiral S-shaped clusters, Fig. 2a ($\omega t = 20$). Due to clockwise rotation, particles preferentially bond at the leading edge of the rotating clusters, where the swept area is larger than the interior, Fig. 2b. Statistics on bond angle θ reveals a peak at around 140°, Fig. 2c. Despite of unclear mechanism, this characteristic $\theta \approx 140°$ is unique to spinner gels and is not observed in colloidal gels. Under the sweep-growth mode described above, a constant $\theta = 140°$ yields a cluster size of $N_{clu} \approx 10$ particles (Fig. 2c, inset), beyond which additional bonds tend to grow inward (dotted lines). This characteristic cluster size can also be estimated geometrically as $2 \times \frac{180°}{180° - 140°} + 1$.

To better characterize structural chirality, we employ the continuous chirality measure (CCM)[37,38]. The dimensionless CCM, ranging from 0 (achiral) to 1 (maximally chiral), gauges the minimal deviation between a structure and its mirror image, accounting for all possible translations, rotations, and permutations (Fig. 2d, inset). Since clusters move as a whole under adhesion, we compute the CCM for each cluster and use a

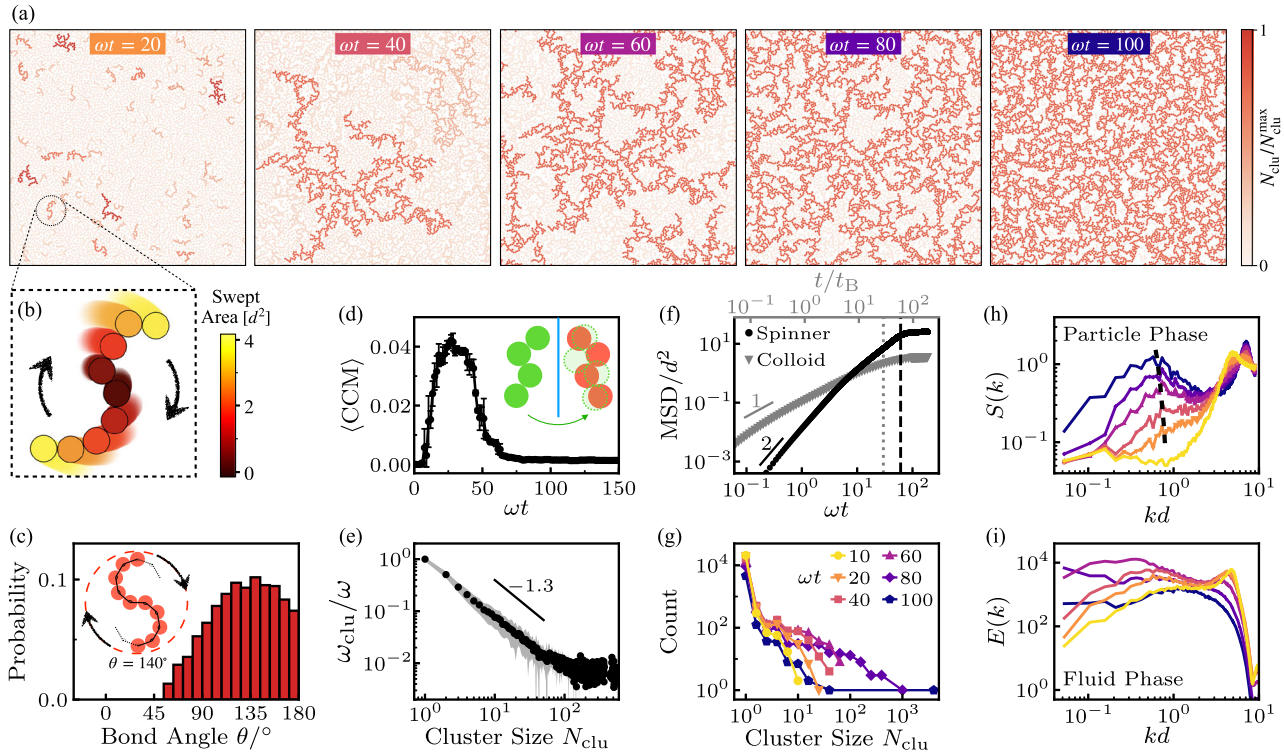

Fig. 2 | Spinner gelation. a Snapshots of spinner gelation at area fraction $\phi = 0.4$ and $\mathrm{Re} = 0.1$ (Supplementary Movie 1). Color indicates normalized cluster size N_{clu}/N_{clu}^{max}. **b** Isolated particles preferably bond to the outer regions of these clusters due to the larger swept area, promoting the growth of S-shaped structures. The color represents the swept area of each particle. **c** Distribution of bond angles θ at $\omega t = 20$. Inset: a typical S-shaped cluster with characteristic bond angle $\theta = 140°$. **d** Global ⟨CCM⟩ (N_{clu}-weighted average Continuous Chirality Measure) evolves over time. Inset: schematic CCM calculation. Using a four-particle cluster (red filled circles) as an example, CCM measures the maximum overlap (green open circles) between its mirror image (green filled circles) and itself upon translations, rotations, and permutations. **e** Mean rotation speed of the cluster ω_{clu} decays with cluster size N_{clu}. Gray region denotes standard deviation. Solid line indicates slope of −1.3. **f** Mean squared displacement (MSD) during colloidal and spinner gelation. Time is normalized by the Brownian time $t_B \equiv \pi\eta d^3/2k_BT$ for colloids and by the spinning frequency ω for spinners. Solid lines indicate slopes of 2 (ballistic) and 1 (diffusive), respectively. Dashed vertical lines denote percolation points. **g** Evolution of the cluster size distribution during spinner gelation. The same color scheme is used in (**g**, **h**). **h** Evolution of the structure factor $S(k)$ computed from the particle configuration. k denotes the wavenumber normalized by particle diameter d. The dashed black line indicates the peak position as a visual guide. **i** Evolution of the energy spectrum $E(k)$ of the flow fields in the x-y plane ($z = 0.5d$), considering only the fluid phase.

N_{clu}-weighted average, ⟨CCM⟩, to represent the global chirality. Initially, ⟨CCM⟩ = 0, since all particles are separated. It then increases rapidly as clustering proceeds, reaches a peak, and starts to decay upon $\omega t \approx 30$ until approaching zero, Fig. 2d. The peak in ⟨CCM⟩ signifies the emergence of transient chirality, predominantly in the form of small, S-shaped clusters. As cluster size N_{clu} increases, the mean $\overline{CCM}$ decreases beyond $N_{clu} \approx 10$ (see Supplementary Note 2), consistent with the characteristic cluster size inferred from bond angle analysis above. Apart from structural features, chirality also manifests in the particle trajectory (see Supplementary Note 3).

The loss of chirality may be explained from two perspectives. While chirality arises from spinning activity, the rotation of the cluster becomes increasingly slow as aggregation proceeds. For a cluster of N_{clu} spinners, it rotates around its center of mass with a total active torque $N_{clu}T_a$. Since the cluster is neither chain-like nor densely packed, its spatial size scales as $l_{clu} \propto {N_{clu}}^{1/d_f}$, where d_f denotes the fractal dimension ($1 < d_f < 2$). Assuming the rotational drag coefficient c_r follows the cubic relation ($c_r \propto {l_{clu}}^3$, see Supplementary Note 4), the cluster's rotational speed is estimated as:

$$\omega_{clu} \propto \frac{N_{clu}T_a}{c_r} \sim {N_{clu}}^{1-3/d_f}. \quad (1)$$

Data extracted from spinner simulations confirms this power-law decay in ω_{clu}, Fig. 2e. The fitted exponent of approximately −1.3 implies a fractal dimension of $d_f \approx 1.3$, consistent with the tenuous clusters in Fig. 2a.

As rotation slows down, structural chirality also becomes less pronounced. Rotational decoherence from the difference in ω_{clu} may further mitigate chirality. Moreover, although individual S-shaped clusters are chiral, subsequent cluster-cluster aggregation randomizes their spatial orientations. This spatial disorder likely contributes to the overall loss of chirality. The growth history of clusters is shown in Fig. 2a. At $\omega t = 40$, transient chirality largely vanishes as clusters merge into larger, more open structures. By $\omega t = 60$, the largest cluster rapidly grows and connects with other clusters, percolating the system. Both visually and quantitatively, the resulting isotropic network exhibits no sign of chirality.

To better investigate the role of spinning, we also simulate passive colloidal gels with Brownian motion ($U_{adh} \gg k_BT$) using the DEM-LBM scheme. Although both systems percolate, their gelation pathways differ. In colloidal gels, particles diffuse until forming a space-spanning network, Fig. 2f (gray), upon which coarsening proceeds slowly (Supplementary Movie 2). Conversely, spinner motion is initially ballistic due to convective flow and transitions to super-diffusion before becoming arrested in a percolating state, Fig. 2f (black). Moreover, clusters in colloidal gels grow uniformly (Supplementary Note 5), with all particles incorporating into the final gel network over time. By contrast, even after percolation, a fraction of isolated monomers remains in the spinner gel, Fig. 2g. As illustrated in Fig. 2a, adhesive spinners tend to percolate first and subsequently undergo internal coarsening, resembling "viscoelastic phase separation gel" formation[39], yet independent of ϕ (Supplementary Note 6). The largest cluster is quite loose at the percolation point (Fig. 2a, $\omega t = 60$), with monomers and small clusters trapped inside enclosed loops. Beyond this

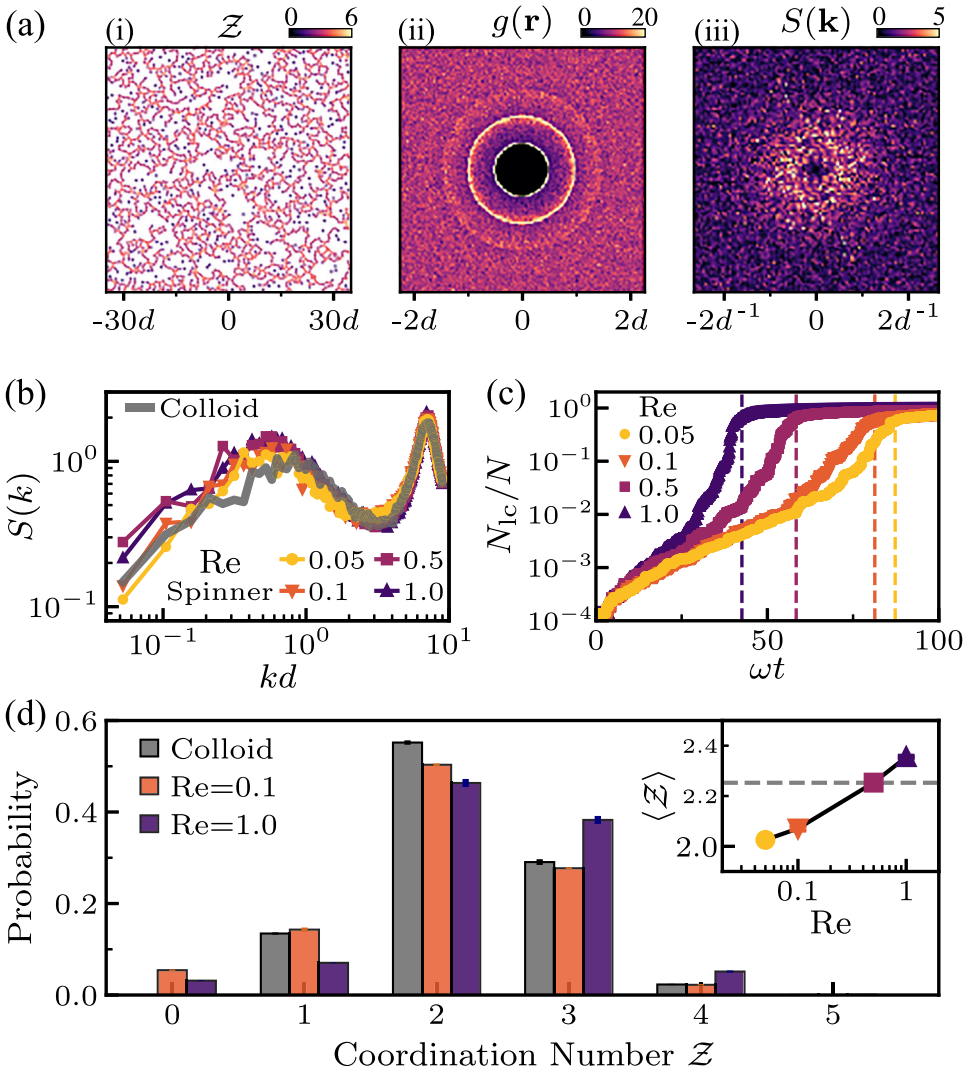

Fig. 3 | Gel structure and dynamics. a Structure of a spinner gel at $\phi = 0.4$ and Re $= 0.1$. (i) Particle configuration, with the color representing coordination number $\mathcal{Z}$. (ii) Pair distribution function, with the color representing intensity. (iii) static structure factor, with the color representing intensity. **b** Radial-averaged structure factors $S(k)$ for a colloidal gel and spinner gels at $\phi = 0.4$. Colored symbols refer to different values of spinning activity Re. The gray line refers to colloids. **c** Evolution of the fraction of particles in the largest cluster N_{lc}/N, for different Re. Dashed lines denote percolation points. **d** Distributions of coordination number $\mathcal{Z}$ for spinner gels at different spinning activities Re and passive colloidal gel, with the same color scheme used in (**b**, **c**). Inset: mean coordination number $\langle\mathcal{Z}\rangle$ as a function of Re (same color scheme). The gray dashed line refers to the colloidal gel.

stage, no visible chirality is retained at large scales, and local configurations become increasingly compact over time.

Colloidal gelation proceeds as an arrested phase separation[27], where a characteristic length scale emerges and grows and gradually stabilizes over time. In the structure factor of spinner gel, nevertheless, a time-invariant length scale $\xi \equiv 2\pi/k_{peak}$ arises from homogeneity and becomes increasingly significant (Fig. 2h) instead of a growing process in typical phase separation (Supplementary Note 5). In contrast with the particle configuration, the energy spectrum of the flow field in the x-y plane indicates a transition in length scale, Fig. 2i. Initially, localized flow fields form around individual spinners. As aggregation progresses, an inverse energy cascade occurs, characterized by a peak shift in $E(k)$ toward lower wavenumbers k, suggesting the emergence of collective flow driven by cluster rotations. While kinetic energy at a large scale becomes increasingly significant, a sudden decay is observed upon percolation, which greatly arrests the motion of both particles (Fig. 2f) and fluid (Fig. 2i).

Structural analysis

Despite their different gelation routes, the final structures of colloidal and spinner gels are quite similar. While the spinner gel configuration appears similarly heterogeneous, multi-scaled, and achiral, both the pair distribution function $g(\mathbf{r})$ and structure factor $S(\mathbf{k})$ are isotropic without evident angular dependence, Fig. 3a. Quantitatively, the structural differences between the two gels are subtle, and their characteristic lengthscales are comparable, Fig. 3b. The fractal dimension at intermediate scales seems to be lower in spinner gels (as indicated by the shallower slope in $S(k)$, Fig. 3b), consistent with that inferred from rotational speed of clusters in Fig. 2e. The distribution of coordination number $\mathcal{Z}$ is also similar between the two systems, Fig. 3d. The main difference lies in the presence of isolated monomers ($\mathcal{Z} = 0$), which are absent in colloidal gels.

The spinning activity T_a, or equivalently the Reynolds number Re, plays little role in the final structure. Within the inertialess regime ($0.05 \le \mathrm{Re} \le 1.0$), the structure factors are nearly identical, as shown in Fig. 3b, with only a slight difference in the large-scale homogeneity. At the particle level, an increase in Re leads to a higher fraction of bonded spinners, Fig. 3d. As activity increases, the number of monomers decreases, while the fraction of particles with coordination number $\mathcal{Z} \ge 3$ (i.e., the branching point[2]) increases as shown in Fig. 3d. In general, higher spinning activity results in a greater average coordination number $\langle\mathcal{Z}\rangle$, Fig. 3d (inset). Similarly, the distribution of local area fraction (from Voronoi analysis) also presents more compact regions in Re $= 1.0$ spinner gel than those in Re $=$ 0.1 (see Supplementary Note 7). The rolling and sliding constraints in this work are implemented through a modified Coulomb model with a friction coefficient $\mu = 1$ (see "Methods"). While small T_a leads to the global rotation of clusters, it is easier for large T_a to overcome the constraints and result in local rearrangement and densification.

Despite the structural similarities, gelation dynamics exhibits a clear dependence on Re. As spinning becomes faster, clustering and gelation also accelerate. While this is expected as the flow velocity is, in principle, proportional to the spinning speed ω, normalizing time by ω^{-1} does not collapse

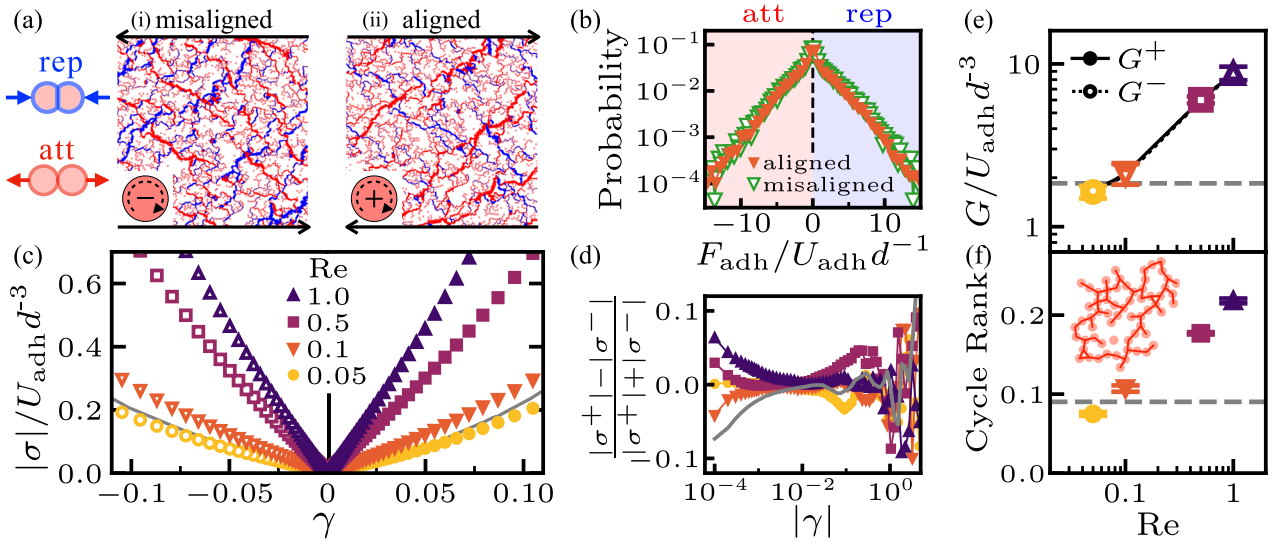

Fig. 4 | Rheology and topology. a Force chains under shear at $\gamma = -0.1$ (i, misaligned shear where the applied shear opposes the spinning direction, denoted as $-$) and $\gamma = 0.1$ (ii, aligned shear, applied in the same direction as the spinning, denoted as $+$). Red bonds indicate tension (interparticle attraction), which manifests when stretched, while blue bonds represent compression (interparticle repulsion), which manifests when squeezed. Bond width is proportional to the force magnitude. **b** Distributions of adhesive forces (normal component) under aligned and misaligned shear at $|\gamma| = 0.1$. **c** Stress response under shear applied in opposite directions. The solid gray line represents the colloidal gel rheology. **d** Normalized stress differences between aligned and misaligned shear vary as functions of absolute strain $|\gamma|$, with the same color scheme used in (**c**). **e** Elastic modulus G as a function of spinning activity Re, with the same color scheme used in (**c**). Solid symbols, representing aligned ($+$) shear moduli, are overlayed by the open symbols, which denote misaligned ($-$) shear moduli. The gray dashed line represents the colloidal gel modulus. **f** Cycle rank as a function of Re, with the same color scheme used in (**c**). The gray dashed line represents the colloidal gel. Inset: schematic nodes (pink disks) and loops (red bonds).

the growth curves of the largest cluster N_{lc}/N, Fig. 3c. This trend also applies to percolation points (dashed lines), indicating that the acceleration in dynamics exceeds simple linear scaling. A possible explanation is that faster rotation drives spinners to better overcome the lubrication barrier before making contact. This is further supported by the larger coordination number at higher Re = 1.0, Fig. 3d.

Absence of odd rheology

Transient chirality is observed at various spinning speeds Re and concentrations ϕ (Supplementary Note 6), yet none of these chiral structures persist in the final gel, as evidenced by the vanishing $\langle CCM \rangle$ in Fig. 2d. To further confirm the absence of chirality, we measure the shear rheology upon the removal of the active torque T_a. In particular, T_a is turned off after gelation, and the system is allowed to fully relax under overdamped conditions. Once the gels reach equilibrium, steady simple shear with a constant shear rate is separately imposed in two opposite directions (aligned and misaligned, see Fig. 4a). The resulting stress σ is measured as a function of strain γ.

Chiral active matters, such as rotors, naturally exhibit odd mechanical responses, including odd viscosity and odd elasticity[21]. Even without activity, metamaterials with a chiral unit cell could also display abnormal asymmetric rheology with odd component[28,40]. For a spinner gel at Re = 0.1, force transmission remains nearly identical when sheared along different directions at $|\gamma| = 0.1$, Fig. 4a. Statistics on adhesive forces (normal component) F_{adh} also exhibits similar distributions, Fig. 4b. Regardless of spinning activity, the absolute values of the responding stress $|\sigma|$ are almost symmetric, as shown in Fig. 4c. Compared with the stress amplitude, the stress differences between aligned and misaligned shear remain negligibly small (<0.1) and do not present systematic bias (of definite sign), Fig. 4d. The elastic moduli, extracted from linear fits to $\sigma = G\gamma$ at small strain $|\gamma| < 0.01$, show no dependence on the shear direction, Fig. 4e. These results, as well as oscillatory rheology (see Supplementary Note 8), are all consistent with the isotropic gel structure, Fig. 3a. Thus, spinner gels are mechanically achiral, as transient chirality from self-rotation is not "memorized" by dynamical arrest.

Although no odd response is observed, the elastic modulus does depend on spinning activity Re, Fig. 4c. Consistent with the coordination number $\mathcal{Z}$ in Fig. 3d (inset), the modulus increases with Re in a power-law manner with an exponent ≈0.5. Local densification (see Supplementary Note 7) leads to less floppy modes and thereby enhances overall stiffness.

However, at Re = 0.1, the modulus G is comparable to that of the colloidal gel, even though around 5% spinners are isolated (Fig. 3d) and thereby do not contribute to elasticity. Compared with the colloidal gel, the density of branching points is also lower in the spinner gel at Re = 0.1. Thus, a softer spinner gel would be expected in this case. This inconsistency may arise from differences in network topology, which is vital to gel rheology[41,42]. In particular, the cycle rank, denoting the ratio of loops to nodes in a network, accurately captures the modulus variation in our gels, Fig. 4f. Consistent with polymeric systems[43,44], the modulus increases with the cycle rank. At Re = 0.1, the spinner gel displays a cycle rank similar to that of the colloidal gel. Although a higher coordination number (and branching density) in the colloidal gel is expected to increase the modulus, floppy modes associated with large loops (Supplementary Note 9) may counteract this stiffening effect, ultimately leading to similar moduli.

Discussion

We investigate the gelation of adhesive rotors in a quasi-2D monolayer, revealing a distinct "top-down" gelation pathway where percolation precedes inward coarsening. Despite the intrinsic chirality of self-rotation, the final spinner gel remains structurally isotropic, with no persistent chirality or odd mechanical responses. However, the elastic modulus is highly tunable through spinning activity, highlighting the role of active rotation in controlling gel mechanics. The key factor is network topology, where connectivity and loop formation govern rheology. While this work mainly reports a specific concentration ($\phi = 0.4$), the observed trends hold across a range of ϕ from 0.3 to 0.5 (Supplementary Note 6), suggesting generic physics in spinner systems. A preliminary study indicates that the mixture of counter-spinning particles can gel much more rapidly and form a stiffer network than unary spinner gels (Supplementary Note 10).

While the above conclusions are purely drawn from simulations, this setup (adhesive spinners) may be experimentally implemented as follows. The combination of ferromagnetic material (e.g., hematite beads[31,32]) and a rotating magnetic field endows active self-spinning. Under gravity, density-mismatched particles sediment onto the bottom substrate, while adding non-adsorbing polymers (such as polystyrene[45]) could induce short-ranged depletion that drives aggregation. To ensure isotropic adhesion, one may apply a core-shell strategy to fabricate particles—a ferromagnetic core encased in a nonmagnetic shell (e.g., PDMS). A proper shell thickness can minimize magnetic-dipolar interactions and ensure that isotropic depletion dominates at contact. With the potential experimental realizations, our findings contribute to the broader understanding of self-assembled active gels, offering design principles for programmable soft matter and chiral metamaterials.

Methods

LBM

We employ a coupled LBM and DEM framework to simulate active spinners in a Newtonian fluid. The fluid dynamics are governed by the LBM with the Bhatnagar-Gross-Krook (BGK) single-relaxation-time approximation[46], in which the evolution of the distribution function f_i follows:

$$f_i(\mathbf{r}+\mathbf{c}_i\Delta t, t+\Delta t) - f_i(\mathbf{r},t) = -\frac{1}{\tau}[f_i(\mathbf{r},t) - f_i^{\mathrm{eq}}(\mathbf{r},t)], \tag{2}$$

where $\mathbf{c}_i$ are the discrete lattice velocities (D3Q19), τ is the relaxation time, and f_i^{eq} is the local equilibrium distribution.

To account for the presence of solid particles, we adopt the partially saturated cell methods (PSM)[47], where each lattice node contains a local solid volume fraction ε. The post-collision distribution is then given by:

$$f_i^{\mathrm{new}} = (1-\varepsilon) f_i^{\mathrm{fluid}} + \varepsilon f_i^{\mathrm{solid}}, \tag{3}$$

with f_i^{fluid} and f_i^{solid} computed from BGK collisions using the local fluid and solid velocities, respectively. The superposition model, in which f_i^{solid} is formed by linearly combining equilibrium distributions of the fluid and solid phases, is used to improve accuracy near curved or moving boundaries.

The fluid-solid interactions are then communicated to the DEM as hydrodynamic force (and torque), computed through momentum exchange with the surrounding fluid:

$$\mathbf{F}_{\mathrm{hydro}} = \sum_i \mathbf{c}_i \left(f_i^{\mathrm{solid}} - f_i^{\mathrm{fluid}}\right), \tag{4}$$

summed over lattice directions intersecting the particle boundary. Lubrication corrections[48] are applied when interparticle gaps fall below the lattice size, compensating for under-resolved near-field interactions. This coupled DEM-LBM-PSM scheme captures both bulk and local hydrodynamics with high fidelity and efficiency, making it well-suited for studying the collective behavior of active systems.

DEM

The DEM is implemented using LAMMPS[33], where particle dynamics, including both translational and rotational motion, are governed by Newton's laws:

$$\begin{aligned} m\frac{\mathrm{d}\mathbf{v}}{\mathrm{d}t} &= \mathbf{F}_{\mathrm{adh}} + \mathbf{F}_{\mathrm{hydro}} + \mathbf{F}_{\mathrm{lub}}, \\ I\frac{\mathrm{d}\boldsymbol{\omega}}{\mathrm{d}t} &= T_{\mathrm{adh}} + T_{\mathrm{hydro}} + T_{\mathrm{lub}} + T_{\mathrm{a}}, \end{aligned} \tag{5}$$

where m and I denote the mass and moment of inertia of a particle, respectively. The hydrodynamic force $\mathbf{F}_{\mathrm{hydro}}$ and torque T_{hydro}, as well as the lubrication corrections $\mathbf{F}_{\mathrm{lub}}$ and T_{lub}, are computed from the LBM solver. The active torque T_{a}, applied along the $-z$ direction, is constant and drives clockwise self-rotation of individual particles. For passive colloids, we include an additional stochastic force (and torque) based on the fluctuation-dissipation theorem to realize the Brownian motion.

As illustrated in Fig. 1b, the adhesive interaction consists of a radial attraction and tangential constraints. The attraction is modeled using a shifted Hookean spring with stiffness k, acting over a short range $\zeta_{\mathrm{a}} = 0.01d$ beyond the particle surface. This is equivalent to a truncated harmonic potential with a minimum energy of $U_{\mathrm{adh}} = \frac{1}{2}k\zeta_{\mathrm{a}}^2$. Tangential constraints, including sliding and rolling resistance, are modeled by a modified Coulomb friction. In particular, the tangential force is characterized by the same stiffness k and a frictional coefficient $\mu = 1$, expressed as

$$\mathbf{F}_{\mathrm{t}} = -\min\left[\mu(F_{\mathrm{n}} + k\zeta_{\mathrm{a}}), k\Delta_{\mathrm{t}}\right]\frac{\mathbf{v}_{\mathrm{t}}}{||\mathbf{v}_{\mathrm{t}}||}, \tag{6}$$

where F_{n} refers to the normal contact force, Δ_{t} and $\mathbf{v}_{\mathrm{t}}$ to the relative tangential displacement and velocity, respectively. Frictional torque is computed analogously using rolling displacement and angular velocity. See ref. 49 for more details of adhesion models.

Parameterization

Our system consists of spherical particles (of diameter d and mass m) settling down to the bottom of a thin square box (of side lengths $L_{x,y} = 120d$ and height $h = 3d$). A Newtonian fluid (of viscosity η and density ρ) is confined between the top and bottom solid no-slip walls in the z direction. While the hydrodynamics is solved in 3D, the particles are confined to the x-y plane at $z = 0.5d$, forming a quasi-2D monolayer. This setup mimics density-mismatched systems in experiments. Through simulations, we confirm that such confinement yields results nearly identical to those obtained under moderate gravitation. Importantly, this setup avoids complications arising from purely 2D hydrodynamics and provides a fundamental platform for chirality investigation.

The LBM is carried out with a lattice spacing of $\Delta x = 0.25d$ and a dimensionless relaxation time of $\tau = 0.68$. The consequent sound speed c_{s} defines the smallest timescale in the simulation. Hydrodynamics is updated every 100 DEM steps to ensure a balance between accuracy and computational efficiency. Lubrication corrections are applied between particles to account for near-field hydrodynamic interactions unresolved by the lattice. These include pairwise forces and torques arising from different modes of relative motion. To prevent divergence, the lubrication is held constant below an inner cutoff of $10^{-3}d$, while an outer cutoff of Δx ensures that corrections are only applied where lattice resolution fails. While we add lubrication corrections between particles, they are not applied to the particle-wall interactions, which, as we confirm, do not qualitatively change the results.

To ensure overdamped dynamics, we maintain the condition that the characteristic damping time, $m/3\pi\eta d$, remains smaller than the interaction timescale $\sqrt{m/k}$. Both timescales are set to be at least an order of magnitude larger than the sound-crossing time d/c_{s}. The adhesive interaction is modeled using a Hookean spring with stiffness k and interaction range $\zeta_{\mathrm{a}} = 0.01d$, resulting in adhesion energy $U_{\mathrm{adh}} = \frac{1}{2}k\zeta_{\mathrm{a}}^2$. To enforce strong bonding, we ensure that $U_{\mathrm{adh}} \gg T_{\mathrm{a}}$, where T_{a} is the active torque applied to each particle to induce self-rotation. The resulting spinning frequency ω defines a timescale ω^{-1}, which is longer than all other dynamical timescales and thereby leads to quasi-static rotation (low Stokes number) and inertialess conditions ($\mathrm{Re} < 1$).

Initial configurations are generated via Langevin dynamics of hard-sphere colloids with a temporarily enlarged diameter of $1.2d$ to prevent overlap. The system is then evolved for a sufficiently long time to allow stable gelation. For rheological measurements, the system is first relaxed and then sheared under a steady strain rate $\dot{\gamma}$, with $\dot{\gamma}^{-1}$ kept significantly larger than all intrinsic timescales to ensure a quasi-static response.

Data availability

The data that correlate with this study are available from the corresponding authors upon reasonable request.

Code availability

The codes of the computer simulations are available from the corresponding authors upon reasonable request.

Received: 28 April 2025; Accepted: 8 October 2025;
Published online: 19 November 2025

References

1. Lu, P. J. et al. Gelation of particles with short-range attraction. *Nature* **453**, 499–503 (2008).
2. Bantawa, M. et al. The hidden hierarchical nature of soft particulate gels. *Nat. Phys.* **19**, 1178–1184 (2023).
3. Jiang, Y. et al. Filled colloidal gel rheology: strengthening, stiffening, and tunability. *J. Rheol.* **69**, 35–44 (2025).
4. Tsurusawa, H., Leocmach, M., Russo, J. & Tanaka, H. Direct link between mechanical stability in gels and percolation of isostatic particles. *Sci. Adv.* **5**, eaav6090 (2019).
5. Rouwhorst, J., Ness, C., Stoyanov, S., Zaccone, A. & Schall, P. Nonequilibrium continuous phase transition in colloidal gelation with short-range attraction. *Nat. Commun.* **11**, 3558 (2020).
6. Bonn, D., Denn, M. M., Berthier, L., Divoux, T. & Manneville, S. Yield stress materials in soft condensed matter. *Rev. Mod. Phys.* **89**, 035005 (2017).
7. Zaccone, A., Wu, H. & Del Gado, E. Elasticity of arrested short-ranged attractive colloids: homogeneous and heterogeneous glasses. *Phys. Rev. Lett.* **103**, 208301 (2009).
8. Wang, Y., Tateno, M. & Tanaka, H. Distinct elastic properties and their origins in glasses and gels. *Nat. Phys.* **20**, 1171–1179 (2024).
9. Koumakis, N. et al. Tuning colloidal gels by shear. *Soft Matter* **11**, 4640–4648 (2015).
10. Szakasits, M. E., Zhang, W. & Solomon, M. J. Dynamics of fractal cluster gels with embedded active colloids. *Phys. Rev. Lett.* **119**, 058001 (2017).
11. Omar, A. K., Wu, Y., Wang, Z. G. & Brady, J. F. Swimming to stability: structural and dynamical control via active doping. *ACS Nano* **13**, 560–572 (2019).
12. Grober, D. et al. Unconventional colloidal aggregation in chiral bacterial baths. *Nat. Phys.* **19**, 1680–1688 (2023).
13. Pedersen, M. C., Mukherjee, S., Doostmohammadi, A., Mondal, C. & Thijssen, K. Active particles knead three-dimensional gels into open crumbs. *Phys. Rev. Lett.* **133**, 228301 (2024).
14. Zhou, T. & Brady, J. F. Active doping controls the mode of failure in dense colloidal gels. *Proc. Natl. Acad. Sci. USA* **121**, e2407424121 (2024).
15. Nguyen, N. H., Klotsa, D., Engel, M. & Glotzer, S. C. Emergent collective phenomena in a mixture of hard shapes through active rotation. *Phys. Rev. Lett.* **112**, 075701 (2014).
16. Chen, P. et al. Self-propulsion, flocking and chiral active phases from particles spinning at intermediate Reynolds numbers. *Nat. Phys.* **21**, 146–154 (2025).
17. Liebchen, B. & Levis, D. Chiral active matter. *EPL* **139**, 67001 (2022).
18. Tan, T. H. et al. Odd dynamics of living chiral crystals. *Nature* **607**, 287–293 (2022).
19. Han, M. et al. Fluctuating hydrodynamics of chiral active fluids. *Nat. Phys.* **17**, 1260–1269 (2021).
20. Goto, Y. & Tanaka, H. Purely hydrodynamic ordering of rotating disks at a finite Reynolds number. *Nat. Commun.* **6**, 5994 (2015).
21. Fruchart, M., Scheibner, C. & Vitelli, V. Odd viscosity and odd elasticity. *Annu. Rev. Condens. Matter Phys.* **14**, 471–510 (2023).
22. Lou, X. et al. Odd viscosity-induced Hall-like transport of an active chiral fluid. *Proc. Natl. Acad. Sci. USA* **119**, e2201279119 (2022).
23. Zhang, B., Yuan, H., Sokolov, A., de la Cruz, M. O. & Snezhko, A. Polar state reversal in active fluids. *Nat. Phys.* **18**, 154–159 (2022).
24. Poggioli, A. R. & Limmer, D. T. Odd mobility of a passive tracer in a chiral active fluid. *Phys. Rev. Lett.* **130**, 158201 (2023).
25. Yuan, J. & Tanaka, H. Colloid phase separation dynamics driven by chiral turbulent flows. *Phys. Rev. Res.* **6**, 023186 (2024).
26. Najuch, T. & Sun, J. Analysis of two partially-saturated-cell methods for lattice boltzmann simulation of granular suspension rheology. *Comput. Fluids* **189**, 1–12 (2019).
27. Zaccarelli, E. Colloidal gels: equilibrium and non-equilibrium routes. *J. Phys. Condens. Matter* **19**, 323101 (2007).
28. Fernandez-Corbaton, I. et al. New twists of 3d chiral metamaterials. *Adv. Mater.* **31**, 1807742 (2019).
29. Frenzel, T., Kadic, M. & Wegener, M. Three-dimensional mechanical metamaterials with a twist. *Science* **358**, 1072–1074 (2017).
30. Wu, W. et al. Mechanical design and multifunctional applications of chiral mechanical metamaterials: a review. *Mater. Des.* **180**, 107950 (2019).
31. Katuri, J. et al. Control of colloidal cohesive states in active chiral fluids. *Commun. Phys.* **7**, 291 (2024).
32. Massana-Cid, H., Levis, D., Hernández, R. J. H., Pagonabarraga, I. & Tierno, P. Arrested phase separation in chiral fluids of colloidal spinners. *Phys. Rev. Res.* **3**, L042021 (2021).
33. Thompson, A. P. et al. LAMMPS—a flexible simulation tool for particle-based materials modeling at the atomic, meso, and continuum scales. *Comp. Phys. Comm.* **271**, 108171 (2022).
34. Guazzelli, É., Morris, J. F. & Pic, S. *A Physical Introduction to Suspension Dynamics* (*Cambridge Texts in Applied Mathematics*) (Cambridge University Press, 2011).
35. Shen, Z. & Lintuvuori, J. S. Two-phase crystallization in a carpet of inertial spinners. *Phys. Rev. Lett.* **125**, 228002 (2020).
36. Shen, Z. & Lintuvuori, J. S. Collective flows drive cavitation in spinner monolayers. *Phys. Rev. Lett.* **130**, 188202 (2023).
37. Dryzun, C. & Avnir, D. Chirality measures for vectors, matrices, operators and functions. *ChemPhysChem* **12**, 197–205 (2011).
38. Abraham, E. & Nitzan, A. Molecular chirality quantification: tools and benchmarks. *J. Chem. Phys.* **160**, 164104 (2024).
39. Tsurusawa, H., Arai, S. & Tanaka, H. A unique route of colloidal phase separation yields stress-free gels. *Sci. Adv.* **6**, eabb8107 (2020).
40. Karathanasopoulos, N., Dos Reis, F., Reda, H. & Ganghoffer, J.-F. Computing the effective bulk and normal to shear properties of common two-dimensional architectured materials. *Comput. Mater. Sci.* **154**, 284–294 (2018).
41. Nabizadeh, M. et al. Network physics of attractive colloidal gels: resilience, rigidity, and phase diagram. *Proc. Natl. Acad. Sci. USA* **121**, e2316394121 (2024).
42. Smith, A. D., Donley, G. J., Del Gado, E. & Zavala, V. M. Topological data analysis for particulate gels. *ACS Nano* **18**, 28622–28635 (2024).
43. Masubuchi, Y. et al. Phantom-chain simulations for the effect of node functionality on the fracture of star-polymer networks. *Macromolecules* **56**, 9359–9367 (2023).
44. Masubuchi, Y., Ishida, T., Koide, Y. & Uneyama, T. Phantom chain simulations for the fracture of star polymer networks with various strand densities. *Soft Matter* **20**, 7103–7110 (2024).
45. Harich, R. et al. Gravitational collapse of depletion-induced colloidal gels. *Soft Matter* **12**, 4300–4308 (2016).
46. Bhatnagar, P., Gross, E. & Krook, M. A model for collision processes in gases. I. Small amplitude processes in charged and neutral one-component systems. *Phys. Rev.* **94**, 511–525 (1954).
47. Noble, D. & Torczynski, J. A lattice-boltzmann method for partially saturated computational cells. *Int. J. Mod. Phys. C* **9**, 1189–1201 (1998).
48. Nguyen, N.-Q. & Ladd, A. J. C. Lubrication corrections for lattice-boltzmann simulations of particle suspensions. *Phys. Rev. E* **66**, 046708 (2002).
49. Jiang, Y. & Seto, R. Colloidal gelation with non-sticky particles. *Nat. Commun.* **14**, 2773 (2023).

Acknowledgements

The authors thank Zaiyi Shen and Zhiyuan Zhao for fruitful discussions. This work was supported by the National Natural Science Foundation of China

(No. 12404235) and Fundamental Research Funds for the Central Universities (FRF-IDRY-24-001; QNXM20250047).

Author contributions

Y.J. conceived the research. Y.J. and Y.C. carried out the simulations. Y.J., H.L. (Haiquan Li), Y.L., H.L. (Haoran Li), and Y.C. analyzed the data. Y.J. and H.L. (Haiquan Li) wrote the manuscript. All authors discussed the results and contributed to the final version of the manuscript.

Competing interests

The authors declare no competing interests.

Additional information

Supplementary information The online version contains supplementary material available at https://doi.org/10.1038/s42005-025-02362-0.

Correspondence and requests for materials should be addressed to Yujie Jiang.

Peer review information *Communications Physics* Rui Zhang, Mathieu Leocmach, and the other, anonymous, reviewer(s) for their contribution to the peer review of this work. A peer review file is available.